Dual-Module NMM-IEM Machine Learning for Fast Electromagnetic Inversion of Inhomogeneous Scatterers With High Contrasts and Large Electrical Dimensions

Li-Ye Xiao, *Member, IEEE*, Jiawen Li, Feng Han, *Member, IEEE*, Wei Shao, *Member, IEEE*, and Qing Huo Liu, *Fellow, IEEE*

***Abstract*— A dual-module machine learning scheme is proposed to reconstruct inhomogeneous scatterers with high contrasts and large electrical dimensions. The first nonlinear mapping module (NMM) is an extreme learning machine (ELM), which is used to convert the measured scattered fields at the receiver arrays into the preliminary images of the scatterers. The second image-enhancing module (IEM) is a convolutional neural network (CNN), which is used to refine further the images from the NMM to obtain high-accuracy pixel-based model parameter distribution in the inversion domain. Compared with the traditional approximate methods such as backpropagation, the NMM-IEM machine learning can produce the preliminary image with a much higher accuracy but the unknown weight matrices of the ELM are only solved once during training. Hence, the IEM connected to the NMM has a simple architecture and can be trained at a rather low cost. The performance of the proposed dual-module NMM-IEM scheme and the conventional variational Born iterative method is compared in terms of inversion of scatterers with different electrical sizes and contrasts. Meanwhile, the NMM-IEM is also assessed for the inversion of scatterers with high contrasts and large electrical dimensions and experimental data. Finally, the NMM-IEM is compared with the CNNs used in the previous works.**

***Index Terms*— Convolutional neural network (CNN), electromagnetic (EM) inversion, extreme learning machine (ELM), high contrast.**

I. Introduction

ELECTROMAGNETIC (EM) inversion aims to reconstruct model parameters such as permittivity, conductivity, and permeability of unknown objects located inside an inaccessible region by analyzing the scattered fields given the illumination of the domain of interest (DOI) [1]. It has been widely applied in geophysical exploration [2], nondestructive evaluation [3], through-wall imaging [4], medical imaging [5], [6], remote sensing [7], and so on.

Because of the intrinsic nonlinear relationship between the unknown model parameters and measured scattered fields and the ill-posedness of the discretized matrix equations, the inverse scattering methods involve nonlinear optimization and regularization [8]. Therefore, iterative methods are usually adopted to solve the inverse scattering problems. For the commonly used iterative methods such as the Born iterative method (BIM) [9] and its variants, the contrast source inversion (CSI) method [4], [10]–[12], and the subspace optimization method (SOM) [13]–[15], the model parameters of the unknown scatterers could be reconstructed by minimizing the objective function that quantifies the mismatch between the calculated and measured scattered fields iteratively. However, the major drawback of these iterative methods is that they are time-consuming and, thus, not suitable for the real-time reconstruction.

In weak scattering scenarios, an inverse scattering problem can also be solved approximately by noniterative methods. For example, the inverse problems can be formulated by the linear equations, which can be solved without iteration by the Born approximation (BA) (including the backpropagation (BP) method [16]) and the extended BA methods [17], [18]. The noniterative methods provide reconstruction results in a quite short-time period, but they are not accurate, especially for strong scattering applications.

In recent years, machine learning has attracted increased attention in the areas of image processing and computer vision, such as image classification [19], [20] and segmentation [21], [22], depth estimation [23], and so on. Methodologies based on the artificial neural network have also been proposed and used to extract rather general information about the geometric and EM properties of the scatterers [24], [25]. Nevertheless, these methods used a few parameters to represent the scatterers, such as their positions, sizes, shapes, and piecewise constant permittivities. The scope of this kind of parameterization is limited, since the scatterers in the DOI can be spatially inhomogeneous and their numbers can be arbitrary. A more

Manuscript received January 8, 2020; revised March 24, 2020; accepted April 16, 2020. Date of publication April 30, 2020; date of current version August 4, 2020. This work was supported in part by the National Key Research and Development Program of China under Grant 2018YFC0603503 and Grant 2018YFF01013300, in part by the National Postdoctoral Program for Innovative Talents under Grant BX2019018, and in part by the National Natural Science Foundation of China under Grant 61871462. *(Corresponding authors: Qing Huo Liu; Feng Han.)*

Li-Ye Xiao, Jiawen Li, and Feng Han are with the Institute of Electromagnetics and Acoustics, Xiamen University, Xiamen 361005, China, and also with the Fujian Provincial Key Laboratory of Electromagnetic Wave Science and Detection Technology, Xiamen University, Xiamen 361005, China (e-mail: liyexiao16@gmail.com; feng.han@xmu.edu.cn).

Wei Shao is with the School of Physics, University of Electronic Science and Technology of China, Chengdu 610054, China (e-mail: weishao@uestc.edu.cn).

Qing Huo Liu is with the Department of Electrical and Computer Engineering, Duke University, Durham, NC 27708 USA (e-mail: qhliu@duke.edu).

Color versions of one or more of the figures in this article are available online at http://ieeexplore.ieee.org.

Digital Object Identifier 10.1109/TAP.2020.2990222

0018-926X © 2020 IEEE. Personal use is permitted, but republication/redistribution requires IEEE permission.
See https://www.ieee.org/publications/rights/index.html for more information.

versatile approach to represent the scatterers is using the pixel basis, i.e., the values of the dielectric parameters in all the pixels are independent of each other. For the pixel-based EM inversion, a novel deep neural network architecture, termed DeepNIS, was proposed in [26]. DeepNIS consists of a cascade of three convolutional neural network (CNN) modules, in which the inputs are the complex-valued images generated by the BP algorithm and the outputs are the super-resolution images of the dielectric parameter distribution of the unknown objects. The DeepNIS outperforms conventional nonlinear inverse scattering methods remarkably in terms of both the reconstruction accuracy and computational time. In [27], three inversion schemes based on the U-Net CNN were proposed for inverse scattering problems. They are the direct inversion scheme, the BP scheme, and the dominant current scheme. In terms of the results of several representative tests, the proposed dominant current scheme outperforms the other two schemes. Both the DeepNIS in [26] and the BP and dominant current schemes in [27] require the pixel-based input images of the scatterer model parameters, which are obtained through the linearized approximation of the inverse scattering problems. When the contrasts of the scatterers are high or their electrical sizes are large, linearized approximation methods may fail. In addition, the direct inversion scheme in [27] can reconstruct the model parameter distribution from the scattered field data directly, although the U-Net spends high cost to train and learn the underlying wave physics. Recently, some improved supervised machine learning techniques have been developed for full-wave EM inversion. For example, in [28], several strategies to incorporate the physical expertise inspired by the traditional iterative algorithms such as CSI and SOM were adopted and the inversion accuracy and efficiency were validated. Yao *et al.* [29] developed a two-step deep learning approach that can reconstruct the high-contrast objects using the cascade of a CNN and another complex-valued deep residual CNN. In [30], the supervised descent learning module is embedded inside the iterative process. The reconstruction of 2-D images was achieved through iterations based on the descent directions learned in the training stage.

In this article, a tailored machine learning scheme composed of two cascaded modules is proposed to reconstruct pixel-based inhomogeneous scatterers with high contrasts and/or large dimensions. The first one is the nonlinear mapping module (NMM) that converts the scattered fields measured at the receiver arrays into the preliminary images of the model parameters in the inversion domain by using a complex-valued extreme learning machine (ELM). The second one is the image-enhancing module (IEM) that further refines the results from the NMM to obtain high-accuracy pixel-based model parameter distribution by using a CNN. Without relying on the conventional nonlinear inversion methods such as BIM, distorted BIM (DBIM), variational BIM (VBIM), CSI, and SOM, the proposed dual-module NMM-IEM machine learning technique could successfully reconstruct the pixel-based model parameters from the measured scattered field data with high accuracy, especially for the scatterers with high contrasts and/or large electrical dimensions. This dual-module scheme is different from the cascaded network proposed in [29], since the

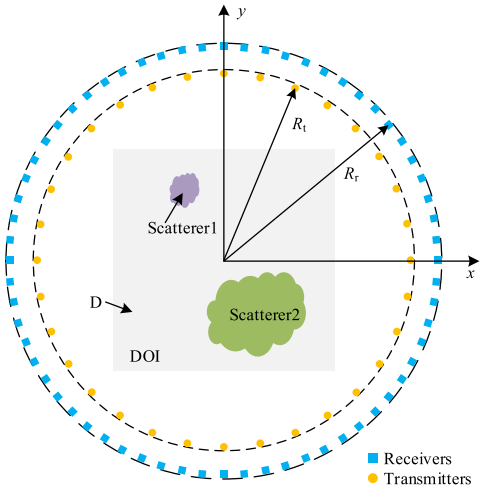

Fig. 1. Typical measurement configuration for a 2-D inverse scattering problem. Transmitters and receivers surrounding the scatterers are placed on the circles with the radii of R_t and R_r, respectively.

ELM is employed in this article. The ELM is a feedforward neural network and is suitable for nondifferential activation functions. To a large extent, it has the advantage of preventing some troubling issues of a neural network such as stopping criteria, learning rate, training epochs, and local minima [31]. The proposed scheme is also different from DeepNIS in [26] and the BP and dominant current schemes in [27], since the preliminary images of the model parameters in these three schemes are obtained by linear approximations, e.g., BP. As a result, strong scattering will cause large errors. By contrast, the NMM in the dual-module scheme can account for the strong nonlinear relationship between the model parameters and the scattered field data. In addition, because the NMM can retrieve the preliminary images with higher accuracy compared with linear approximations, the training of the following CNN in the IEM has a low cost due to its simple architecture. Our method is also different from the direct inversion scheme in [27]. The scattered field data are directly converted into the final model parameters in the direct inversion scheme. The physics of EM scattering is included in the training and learning of the CNN in the direct inversion scheme. In our dual-module scheme, the scattered field data are mapped to the preliminary images of the model parameters through the nonlinear transform of the ELM. Compared with the conventional CNN, e.g., U-Net that uses the gradient-based learning algorithms to tune iteratively the network parameters, the ELM randomly chooses the hidden nodes and analytically determines the output weights for the hidden layers of the feedforward neural networks, which has the much lower training cost than the traditional feedforward neural networks. However, previous numerical experiments showed that the ELM has a good generalization performance in most cases [31]. In addition, numerical cases in this article show that the ELM of the NMM can well reflect the strong nonlinear effects of EM scattering by scatterers with high contrasts and/or large electrical dimensions although it has a simple architecture and its unknown model weights are only solved once. Compared

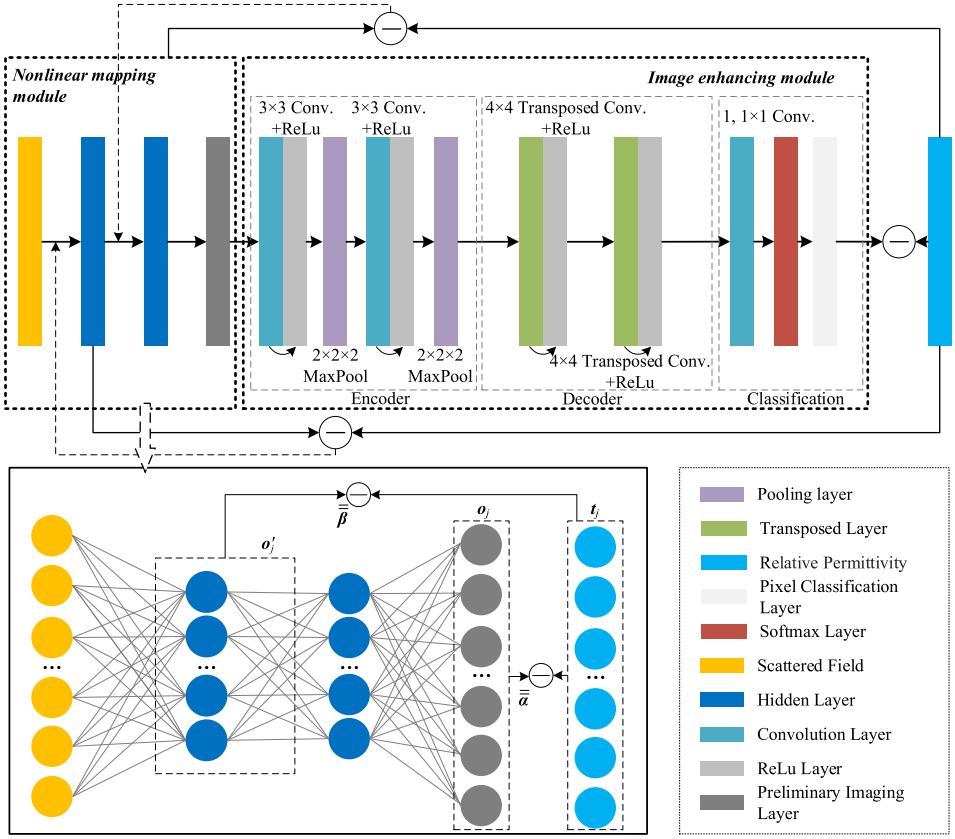

Fig. 2. Architecture of the dual-module NMM-IEM machine learning scheme. It includes two parts: the NMM and the IEM.

with previous research work, this article has the following novelties: 1) scatterers with high contrasts and large electrical dimensions can be reconstructed by the machine learning scheme very quickly and 2) the training of the ELM and the CNN has the low costs.

This article is organized as follows. In Section II, the formulation of the inverse scattering problems based on integral equations is introduced. In Section III, the NMM and IEM are discussed in detail. In Section IV, numerical results are presented. The inversion performance of the proposed dual-module NMM-IEM scheme and VBIM is compared. In Section V, the measured data in laboratory experiments are reconstructed by the NMM-IEM. Finally, the conclusions are drawn in Section VI.

II. Conventional Solutions of the EM Inverse Scattering Problems

In this section, we briefly describe the conventional forward and inverse scattering formulas. As shown in Fig. 1, several 2-D scatterers are placed in the free space. Transmitters and receivers surrounding the scatterers are $\hat{z}$-polarized. When the integral equation method is adopted, the forward scattering model is formulated by the state equation

$$E_z^{inc}(\boldsymbol{\rho}) = E_z^{tot}(\boldsymbol{\rho}) + \frac{jk_0^2}{4}\int_D \chi_\varepsilon(\boldsymbol{\rho}')E_z^{tot}(\boldsymbol{\rho}')H_0^{(2)}(k_0|\boldsymbol{\rho}-\boldsymbol{\rho}'|)d\boldsymbol{\rho}' \tag{1}$$

where E_z^{inc} is the incident electric field when the scatterers in the DOI are absent, while E_z^{tot} is the total electric field when the scatterers are present. k_0 is the wavenumber in free space and $H_0^{(2)}$ is the zeroth-order Hankel function of the second kind. The contrast χ_ε is expressed as

$$\chi_\varepsilon(\boldsymbol{\rho}) = \varepsilon_r(\boldsymbol{\rho}) - 1. \tag{2}$$

Equation (1) can be discretized using the 2-D mixed-order basis functions and solved by the stabilized biconjugate-gradient fast Fourier transform (BCGS-FFT) method. The details can be found in [32] and will not be repeated here.

The inverse scattering model is formulated by the data equations

$$E_z^{sct}(\boldsymbol{\rho}) = -\frac{jk_0^2}{4}\int_D \chi_\varepsilon(\boldsymbol{\rho}')E_z^{tot}(\boldsymbol{\rho}')H_0^{(2)}(k_0|\boldsymbol{\rho}-\boldsymbol{\rho}'|)d\boldsymbol{\rho}' \tag{3a}$$

$$\mathbf{H}^{sct}(\boldsymbol{\rho}) = \frac{k_0\omega\varepsilon_0}{4}\hat{z} \times \int_D \frac{\boldsymbol{\rho}-\boldsymbol{\rho}'}{|\boldsymbol{\rho}-\boldsymbol{\rho}'|}\chi_\varepsilon(\boldsymbol{\rho}')E_z^{tot}(\boldsymbol{\rho}')H_1^{(2)}(k_0|\boldsymbol{\rho}-\boldsymbol{\rho}'|)d\boldsymbol{\rho}' \tag{3b}$$

where $H_1^{(2)}$ is the first-order Hankel function of the second kind. Solving the data equations (3) is to map the data vector of the discretized E_z^{sct}, H_x^{sct}, and H_y^{sct} measured at the receivers to the pixel-based 2-D image of $\varepsilon_r(\boldsymbol{\rho})$ distribution in the inversion domain. Because E_z^{tot} also depends on ε_r, such a mapping is nonlinear. In the conventional way, the total

field and the contrast are updated alternately by solving the state equation (1) and data equations (3) alternately. Although several iterative solvers, such as VBIM [32], subspace-based optimization method [13], and CSI [4], are proposed to accommodate the nonlinear relationship between the scattered field and the contrast, the computational cost is high. Some linear solvers such as BA and extended BA run fast but only work for scatterers with low contrasts or small electrical sizes. Therefore, it is desirable to develop a fast solver to account for the strong nonlinear relationship between the scattered field and the contrast in the inversion domain.

In this article, we use the NMM containing an ELM to realize the nonlinear mapping from the scattered field data to the pixel-based permittivity distribution. Although the NMM has a simple architecture and a low training cost, it can recover the preliminary images of the scatterers with high contrasts and/or large dimensions from the scattered field data quickly. The performance of the proposed NMM and the BA solver is compared in Section IV. One should note that we use BA for the test instead of using BP, as BP can be viewed as a special case of BA [33]. In addition, following the NMM is the IEM that will further improve the inversion results.

III. Dual-Module NMM-IEM Machine Learning

There are two parts in the proposed dual-module NMM-IEM machine learning model: the NMM and the IEM. The NMM is employed to preliminarily convert the complex-valued scattered field data into the real-valued relative permittivity in the DOI. The IEM as a CNN is used to enhance further the reconstructed image from the NMM. Fig. 2 shows the architecture of the proposed method.

A. NMM

The scattered fields measured at the receiver arrays are complex-valued data, while the relative permittivity of the DOI is the real value. The NMM is to convert the complex-valued scattered field data into the real permittivity with their nonlinear relationship manifested by the EML that has a simple architecture with low training cost. The NMM has four layers: the input layer, two hidden layers, and the preliminary imaging layer. The input layer nodes are filled with the column vector $\mathbf{x}_j = [x_{1j}, x_{2j}, \ldots, x_{Mj}]^T \in \mathbf{C}^M$, which contains the complex-valued E_z^{sct}, $\eta_0 H_x^{sct}$, and $\eta_0 H_y^{sct}$ for all the transmitter and receiver combinations, where η_0 is the intrinsic impedance of free space. The combination of E_z^{sct}, $\eta_0 H_x^{sct}$, and $\eta_0 H_y^{sct}$ could increase the diversity of the training data through the random matrix in the ELM to obtain more reliable reconstruction results. The subscript j denotes the jth training data set and M is the dimension of the input data set for each training. The NMM output column vector $\mathbf{o}_j = [o_{1j}, o_{2j}, \ldots, o_{Nj}]^T \in \mathbf{R}^N$ has real values, and its dimension N is the total pixel number in the DOI. It is evaluated by

$$\mathbf{o}_j = \overline{\overline{\boldsymbol{\alpha}}} g_r(\overline{\overline{\boldsymbol{w}}}_r | \overline{\overline{\boldsymbol{\beta}}} g_c(\overline{\overline{\boldsymbol{w}}}_c \mathbf{x}_j + \mathbf{b}) | + \mathbf{p}) \tag{4}$$

where $j = 1, 2, \ldots, P$ if there are totally P sets of training data. $\overline{\overline{\boldsymbol{w}}}_c$ is an $L \times M$ complex-valued random weight matrix, and $\mathbf{b}$ is a column threshold vector including L complex-valued random numbers [31]. g_c is the nonlinear activation function, and its outputs are the L complex values in the neurons of the first hidden layer. $\overline{\overline{\boldsymbol{\beta}}}$ is a $K \times L$ complex-valued weight matrix connecting the neurons of the first hidden layer to the inputs of the second hidden layer and K is the neuron connection numbers to the output layer. It is determined by training. $\overline{\overline{\boldsymbol{\alpha}}}$, g_r, $\overline{\overline{\boldsymbol{w}}}_r$, and $\mathbf{p}$ play the similar parts as $\overline{\overline{\boldsymbol{\beta}}}$, g_c, $\overline{\overline{\boldsymbol{w}}}_c$, and $\mathbf{b}$, respectively, but work for the second hidden layer and have real values. $\overline{\overline{\boldsymbol{\alpha}}}$ connects the neurons of the second hidden layer and the nodes in the preliminary imaging layer. The dimensions of $\overline{\overline{\boldsymbol{\alpha}}}$, $\overline{\overline{\boldsymbol{w}}}_r$, and $\mathbf{p}$ are $N \times S$, $S \times K$, and S, respectively.

With many times of experiments in this article, an inverse hyperbolic function expressed as

$$g_c = \operatorname{arcsinh}(x) = \int_0^x \frac{dt}{\sqrt{1+t^2}} \tag{5}$$

is selected as the complex activation function g_c, and the sigmoid function expressed as

$$g_r = \operatorname{sigmoid}(x) = \frac{1}{1+e^{-x}} \tag{6}$$

is selected as the real activation function g_r. It is assumed that the true relative permittivity values in the DOI are denoted as $\mathbf{t}_j = [t_{1j}, t_{2j}, \ldots, t_{Nj}]^T \in \mathbf{R}^N$. To obtain the optimum $\overline{\overline{\boldsymbol{\beta}}}$, we minimize the mismatch between the inputs of the second hidden layer and the true relative permittivity values, i.e., we let $\sum_{j=1}^{P} \| \mathbf{o}'_j - \mathbf{t}_j \| = 0$ and solve for the complex-valued weight matrix $\overline{\overline{\boldsymbol{\beta}}}$. The real-valued weight $\overline{\overline{\boldsymbol{\alpha}}}$ can be obtained following the similar procedure by minimizing the mismatch between the node values of the preliminary imaging and $\mathbf{t}_j$ for all the training data sets, i.e., we let $\sum_{j=1}^{P} \| \mathbf{o}_j - \mathbf{t}_j \| = 0$. Meanwhile, to satisfy the dimension matches for different vectors and matrices, we set $K = N$. Thus, the equation relating the weight matrix $\overline{\overline{\boldsymbol{\beta}}}$ of the first hidden layer to the true relative permittivity vector $\mathbf{t}_j$ for all the training data sets can be compactly expressed as

$$\overline{\overline{\boldsymbol{\beta}}}\,\overline{\overline{\mathbf{G}}}_c = \overline{\overline{\mathbf{T}}} \tag{7}$$

where $\overline{\overline{\mathbf{T}}} = [\mathbf{t}_1; \mathbf{t}_2; \ldots; \mathbf{t}_P]_{N \times P}$ and $\overline{\overline{\mathbf{G}}}_c$ is the combination of all the column vector output from the activation function g_c of the first hidden layer for all the training data sets $\overline{\mathbf{x}}_j$ and has the dimensions of $L \times P$. Thus, the optimum complex-valued weight matrix $\overline{\overline{\boldsymbol{\beta}}}$ could be computed by

$$\hat{\overline{\overline{\boldsymbol{\beta}}}} = \overline{\overline{\mathbf{T}}}\,\overline{\overline{\mathbf{G}}}_c^{\dagger} \tag{8}$$

where the complex matrix $\overline{\overline{\mathbf{G}}}_c^{\dagger}$ is the Moore–Penrose generalized inverse of the complex matrix $\overline{\overline{\mathbf{G}}}_c$. The computation of the Moore–Penrose generalized inverse could be referred from [34]. Following the similar procedure, we can obtain the optimum real matrix:

$$\hat{\overline{\overline{\boldsymbol{\alpha}}}} = \overline{\overline{\mathbf{T}}}\,\overline{\overline{\mathbf{G}}}_r^{\dagger} \tag{9}$$

where the real-valued matrix $\overline{\overline{\mathbf{G}}}_r$ is the combination of all the column vector output from the activation function g_r of

the second hidden layer and has the dimensions of $S \times P$. We can see that the ELM in the NMM can be trained at a low cost, since both unknown weight matrices of two hidden layers can be obtained by solving the matrix inverse only once.

B. IEM

The IEM is used to improve further the 2-D image output from the NMM. It is actually a CNN and consists of an encoder, a decoder, and a pixel classifier. The encoder is employed to analyze and contract the input data, and then, the decoder synthesizes and expands the previously encoded feature. Finally, the decoded output is the input to the pixel classifier for a full-resolution segmentation. As shown in Fig. 2, there are two layers in the encoder, two layers in the decoder, and one layer in the pixel classifier. In each layer of the encoder, a convolution kernel with the size of 3×3 and a rectified linear unit (ReLu) are followed by a 2×2 max pooling. In the decoder, each layer consists of a transposed convolution kernel with the size of 4×4 and an ReLu. Following the decoder, the convolution with the 1×1 kernel size produces the output with one channel. Then, a pixel classifier is employed to classify each pixel of the image for a full-resolution segmentation. Since the CNN is quite mature and discussed a lot in previous literature and has been successfully applied to image segmentation for the full-wave inversion [26], [27], [35], we will not discuss it further here. In addition, because the NMM can recover the preliminary images of the scatterers with higher accuracy than BA or BP, the training cost of the CNN in the IEM is lowered accordingly. In addition, this will be verified in Section VI.

IV. Numerical Results

In this section, two numerical examples are presented. The first one is used to validate the feasibility of the dual-module NMM-IEM machine learning scheme, and its implementation efficiency and accuracy are also compared with those of the conventional VBIM method. In the second example, the reconstruction of the scatterers with high contrasts and/or large dimensions is performed and the antinoise ability of the NMM-IEM is also evaluated. In both examples, the training model is the same. It is the variant of the "Austria" profile [4]. All simulations are performed on a personal computer with an Intel i7-9700 3.00 GHz CPU and 64 GB RAM. When the contrasts of the scatterers are too high, it is not feasible to use the BCGS-FFT presented in [32] to solve the integral equations to obtain the scattered fields. Therefore, the commercial software COMSOL using the finite-element method synthesizes the scattered field data that will be used for training and testing in the following.

A. EM Inversion Setups

In both numerical examples, the operating frequency is 300 MHz, corresponding to a wavelength of $\lambda_0 = 1$ m in free space. Following the Nyquist sampling theorem that the spatial distance between two receivers should roughly be half wavelength, 40 transmitters and 60 receivers are uniformly placed on two concentric circles with the radii of 4 and 4.5 m, respectively. The DOI shown in Fig. 3 has the size of 5 m $\times$ 5 m and is discretized into 96×96 pixels with its center at the origin. To evaluate quantitatively the reconstruction performance, we define the model misfit and data misfit under the L_2 norm as

$$\mathrm{Err}_{\mathrm{model}} = \frac{\|\mathbf{md}_R - \mathbf{md}_T\|}{\|\mathbf{md}_T\|} \tag{10}$$

$$\mathrm{Err}_{\mathrm{data}} = \frac{\|\mathbf{da}_R - \mathbf{da}_T\|}{\|\mathbf{da}_T\|} \tag{11}$$

where $\mathbf{md}_T$ is the vector of the true model parameter values in all the pixels and $\mathbf{md}_R$ is the reconstructed model parameter vector; $\mathbf{da}_T$ is the vector of the measured scattered field data collected at all the receivers and $\mathbf{da}_R$ is the reconstructed scattered field data vector.

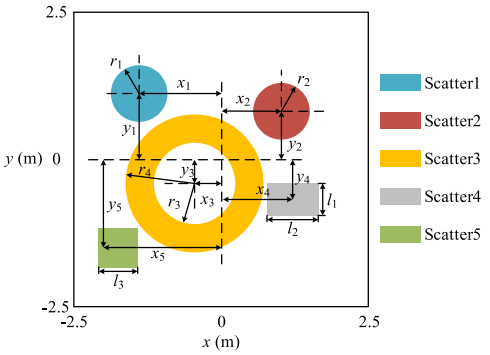

Fig. 3. 2-D training and testing model, which is the variant of the "Austria" profile.

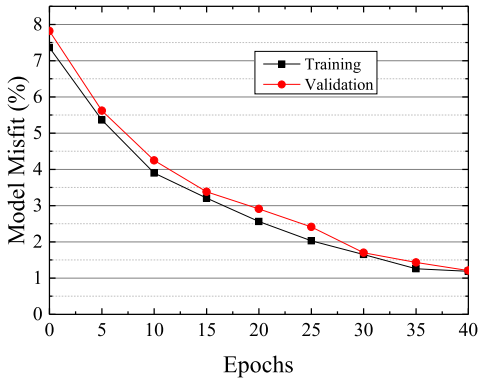

Fig. 4. Variations of model misfits in the training and validation of IEM. The training terminates when the misfit approaches 1%.

B. Training Details of Two Modules

We use the variant of the "Austria" profile to train the NMM and the IEM. As shown in Fig. 3, the radii and centers of both disks, i.e., r_1, r_2, x_1, y_1, x_2, and y_2, and the inner and outer radii and centers of the ring, i.e., r_3, r_4, x_3, and y_3, are set as variables and assigned random values with their ranges listed in Table I. Meanwhile, to enrich the training data sets, we add a rectangle and a square to the DOI. The centers of the rectangle and square, i.e., x_4, y_4, x_5, and y_5, and the side lengths of these two shapes, i.e., l_1, l_2, and l_3, are also set as variables

TABLE I

PARAMETER RANGES FOR THE SCATTERERS IN THE INVERSION MODEL SHOWN IN FIG. 3

Parameter / Range	r_1	x_1	y_1	r_2	x_2	y_2	r_3	r_4	x_3	y_3	l_1	l_2	x_4	y_4	l_3	x_5	y_5	ε_1	ε_2	ε_3	ε_4	ε_5
Minimum	0.1	-2	-2	0.1	-2	-2	0.1	0.2	-2	-2	0.1	0.1	-2	-2	0.1	-2	-2	1	1	1	1	1
Maximum	1	2	2	1	2	2	1	2	2	2	2	2	2	2	2	2	2	8	8	8	8	8

Remark: the unit of length is meter. ε_i is the relative permittivity value of ith scatterer.

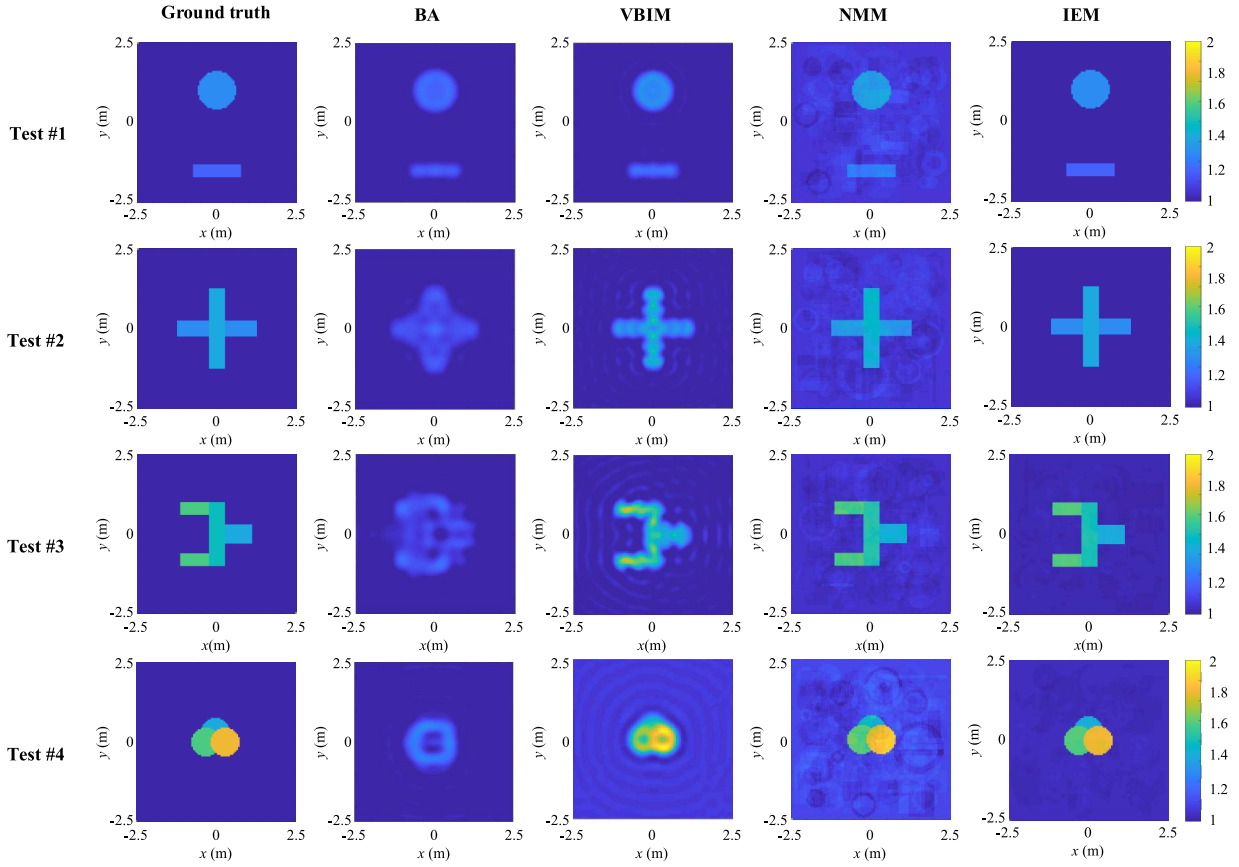

Fig. 5. Four inhomogeneous scatterers are used to test the proposed dual-module machine learning scheme. From the first row to the fourth row, both the geometric shape complexity and contrasts increase. The first column is the ground truth, and from the second column to the fifth column, the inversion results from BA, VBIM, NMM, and IEM are shown, respectively.

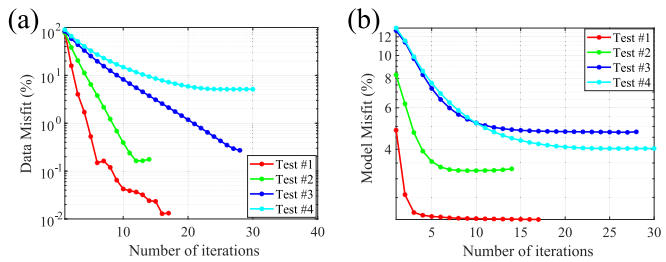

Fig. 6. Variations of (a) data misfits and (b) model misfits in the VBIM iterations.

and assigned random values. The relative permittivities of the five scatterers are randomly set with different values in the range of [1, 8]. Hundred randomly generated training samples are employed to train the NMM. The Hecht–Nelson method is used to calculate the node number of the two hidden layers [36]. When there are n sets of training data, the node number of the hidden layer is empirically chosen as $2n+1$. Therefore, in the NMM, the dimensions of $\overline{\overline{\boldsymbol{\beta}}}$ and $\overline{\overline{\boldsymbol{\alpha}}}$ are 9216 × 201. Within 1 s, the values of $\hat{\overline{\overline{\boldsymbol{\beta}}}}$ and $\hat{\overline{\overline{\boldsymbol{\alpha}}}}$ could be obtained. The 100 sets of outputs from the NMM are used as the inputs to train and validate the IEM. Among them, 75 sets are used for training and 25 sets for validation. As shown in Fig. 4, after 40 epochs, the model misfit approaches 1%, and then, the training process terminates.

C. Comparisons With Conventional Inversion Methods

To validate the inversion accuracy and efficiency of the dual-module NMM-IEM machine learning scheme, we compare their inversion results with those from the conventional BA and VBIM. As shown in Fig. 5, from Tests #1 to #4, the contrast of the scatterer gradually increases. Meanwhile, the geometric shape also becomes more and more complex. For the scatterers in the inversion domain including the simple disk and the rectangle with the low contrasts in Test #1, both BA and VBIM can reconstruct the scatterers well. As the contrast

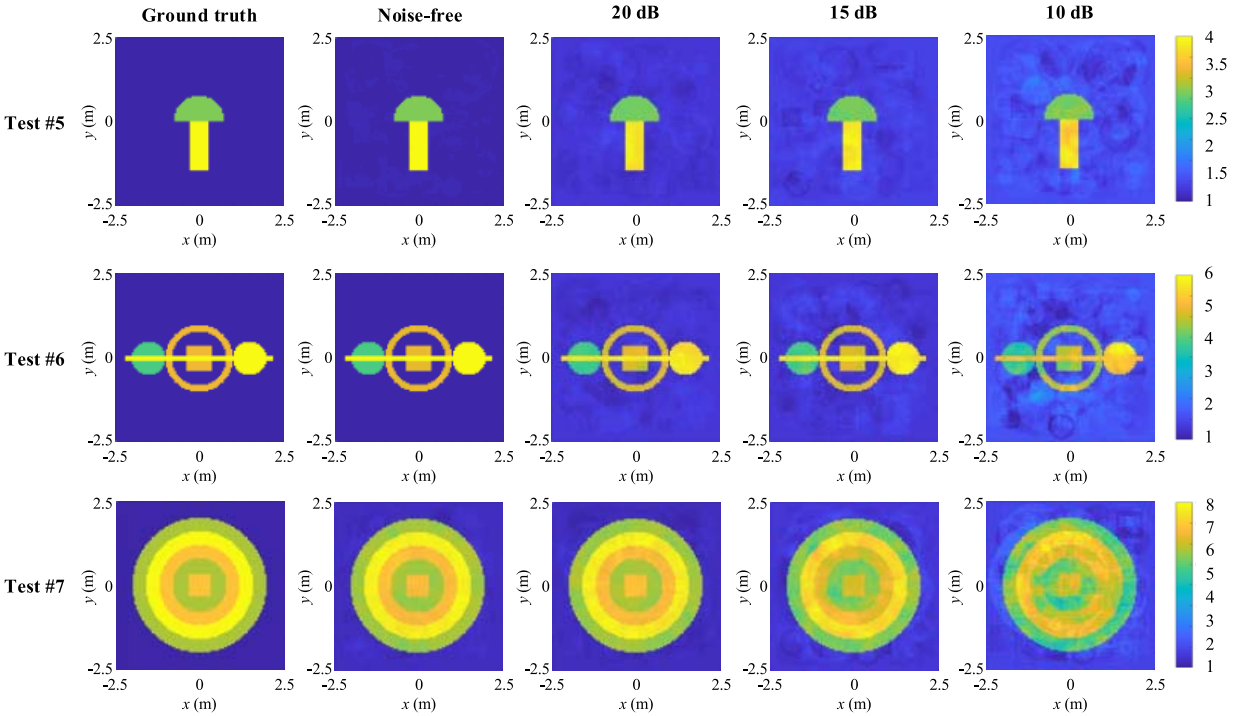

Fig. 7. Three inhomogeneous scatterers with high contrasts and large electrical dimensions are used to test the proposed dual-module machine learning scheme. From the first row to the third row, both the complexity of geometric shapes and contrast increase. The first column is the ground truth, and from the second column to the fifth column, the inversion results of the NMM-IEM for noise-free, 20 dB noise, 15 dB noise, and 10 dB noise are shown, respectively.

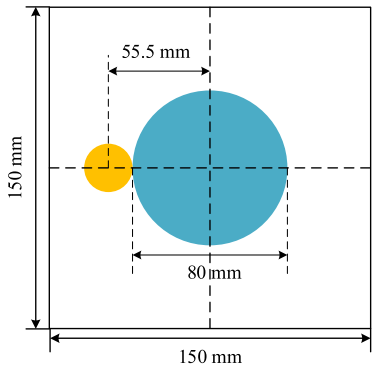

Fig. 8. Inversion domain and the true profile of "FoamDielExt" in the experimental data. The inversion domain has the size of 0.15 m × 0.15 m, and the frequency is at 5 GHz. The large disk scatterer has the diameter of 80 mm, and its relative permittivity is 1.45. The small disk scatterer has the diameter of 31 mm with the relative permittivity of 3.

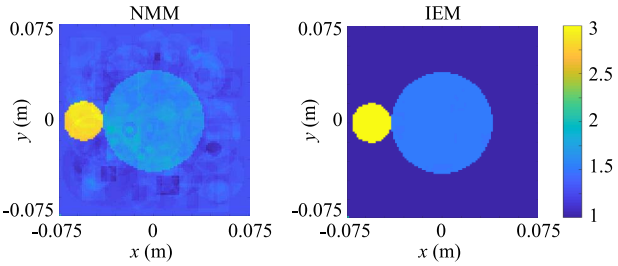

Fig. 9. Reconstructed relative permittivity profiles of "FoamDielExt" by the NMM and IEM.

values increase, the inversion results by BA show larger and larger errors. In Test #4, even the iterative VBIM cannot reconstruct the three overlapped disks. However, the inversion results by the NMM and IEM are almost not affected by different contrast values and shape complexity, which is shown by the fourth and fifth columns of Fig. 5. This is further quantitatively verified by the model misfits listed in Table II. As can been seen, from Tests #1 to #4, the model misfits from BA and VBIM gradually increase. However, they almost remain unchanged for the NMM and the IEM. The IEM further improves the reconstructed images from the NMM by approximately reducing the model misfits by 2%. In addition, one should note that the discrepancies of model misfits between the VBIM and the IEM also gradually increase from Tests #1 to #4. This indicates that the proposed dual-module scheme has stronger adaptability. In other words, it is more competent to deal with the scatterers with high contrasts and complex geometric shapes compared with the conventional VBIM. In addition, we also computed the scattered fields by substituting the reconstructed relative permittivity values in all the pixels into (3) and then evaluated the data misfits. They are 0.0093%, 0.009%, 0.0169%, and 0.362% for Tests #1–#4, respectively.

Fig. 6 shows the variations of data misfits and model misfits for the inversion by VBIM. From Tests #1 to #4, it becomes more and more difficult for the VBIM to converge to a low data misfit. The final data misfit of Test #4 is the largest, while that of Test #1 is the smallest. This is quite different from the stable trend of data misfit values by the NMM-IEM mentioned above. For the model misfits shown in Fig. 6(b), Test #1 also has the smallest value. However, Test #3 has the larger final model misfit than Test #4. This is because the electrical size of the scatterer in Test #3 is larger than that of Test #4 although the contrast value used in Test #3 is smaller. Because each

TABLE II
MODEL MISFITS (%) OF FOUR TESTS SHOWN IN FIG. 5

Test \ Method	BA	VBIM	NMM	IEM
#1	4.8230	2.0181	3.2615	1.0346
#2	8.2708	3.6495	3.3103	1.0951
#3	12.7513	5.5959	3.2916	1.0415
#4	13.0708	4.0328	3.2812	1.0864

TABLE III
CONTRASTS AND MODEL MISFITS (%) OF THREE TESTS SHOWN IN FIG. 7

Test \ Parameter	Largest χ_ϵ	Noise-free	20dB	15dB	10dB
#5	3	1.2516	3.5433	7.2061	15.3315
#6	5	1.2814	3.5549	7.2123	15.3595
#7	7	1.3108	3.7316	7.2161	15.3634

VBIM iteration takes about 46 s in Test #4, the total time cost of VBIM is much higher than that of the dual-module scheme that spends less than 1 s to obtain the final high-accuracy 2-D image. In addition, we also input the reconstructed 2-D images by the NMM in Test #4 into the VBIM solver as the initial values. Then, the VBIM takes around 983 s to obtain the final inversion results that have the model misfit as large as 4.017%. This is around four times of the model misfit by IEM. Obviously, it is inadvisable to replace the IEM module in the proposed scheme with a conventional iterative solver.

D. Inversion of Scatterers With High Contrasts and Large Electrical Dimensions

Then, three scatterers with high contrasts and large electrical dimensions, as shown in Fig. 7, are used to test the proposed dual-module NMM-IEM scheme. From Tests #5 to #7, both the contrasts and dimensions gradually increase. Meanwhile, we add 20, 15, and 10 dB Gaussian white noise to evaluate further the antinoise ability of the proposed method. Here, the noise level is defined by the signal-to-noise ratio (SNR) of power. Test #5 is designed with a tangency semicircle and a rectangle to evaluate the ability of NMM-IEM to distinguish different tangency scatterers, where the largest contrast is 3. The multiple scatterers in Test #6 are tangency, nested and overlapped and have the largest contrast of 5. In Test #7, we select four concentric circles and a square overlapped together and the largest contrast is 7. As shown in Fig. 7, as the noise increases, the reconstructed 2-D images become more and more blurred, which are clearly illustrated by the increasing model misfits listed in Table III. However, the model misfits in three different tests almost keep the same levels for both noise-free and noisy scenarios although both the electrical sizes and the largest contrast χ_ϵ increase from Tests #5 to #7. The evaluated data misfits for the noise-free cases also show the similar stable trend. They are 1.1%, 1.34%, and 1.26% for Tests #5–#7, respectively. Note that the electrical dimensions of DOI here are $5\lambda_0 \times 5\lambda_0$, and in Test #7, the diameter of the largest circle is $4\lambda_0$. Numerical simulations show that the conventional solver such as VBIM does not converge for these three tests. It cannot tackle the scatterers with high contrasts and large electrical dimensions, but the proposed dual-module scheme can.

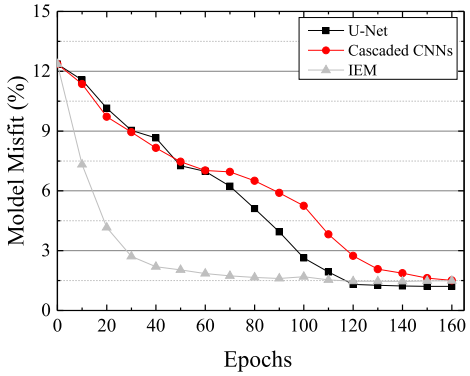

Fig. 10. Variations of model misfits in the training processes of U-net, three cascaded CNNs, and the proposed IEM.

V. TESTS WITH EXPERIMENTAL DATA

The experimental data measured at Institute Fresnel [37] are used to evaluate further the proposed scheme. A "FoamDielExt" profile, as shown in Fig. 8, with the TM case selected, is adopted in the test. In the measurement environment, both the transmitter and receiver arrays are placed on a circle with the radius of 1.67 m surrounding the "FoamDielExt" profile. Eight transmitters are used, and the field data are recorded by 241 receivers. The experimental data are calibrated by multiplying them with a single complex-valued coefficient that is derived from the ratio of the measured incident field and the simulated one at the receiver opposite to the source [37]. Thus, according to the experimental setup, the training data are chosen similar to those in Section IV, with the difference that we downsize the DOI dimensions to 150 mm $\times$ 150 mm, increase the frequency to 5 GHz, and set the range of relative permittivity between 1.0 and 3.5. Hundred samples are produced by COMSOL and employed to train the proposed dual-module scheme, and the measured scattered field data for the "FoamDielExt" profile provided by Institute Fresnel are set as the input of test. Within 1 s, the reconstructed relative permittivity profiles from the NMM and the IEM are obtained and the results are shown in Fig. 9. The model misfits of the NMM and IEM are 3.39% and 1.10%, respectively. Meanwhile, the data misfits for the reconstructed profiles by the NMM and IEM are 9.37% and 3.42%, respectively. The results from the experimental data further verify the effectiveness of the proposed NMM-IEM model that has a good performance when dealing with highly nonlinear inverse scattering problems.

VI. COMPARISONS WITH OTHER CNNS

We compare the proposed dual-module scheme with the U-Net used in [27] and three cascaded CNNs adopted in [26]. Because the preliminary images in [26] and [27] are acquired by BP, we directly compare the IEM in this article with the U-Net in [27] and three cascaded CNNs in [26]. Both the training and testing data sets used for the comparisons are generated by the NMM. The MNIST database [38], which is a database of handwriting digits widely used in the field of machine learning, is employed to represent the inhomogeneous scatterers. The DOI has the dimensions of 2 m $\times$ 2 m.

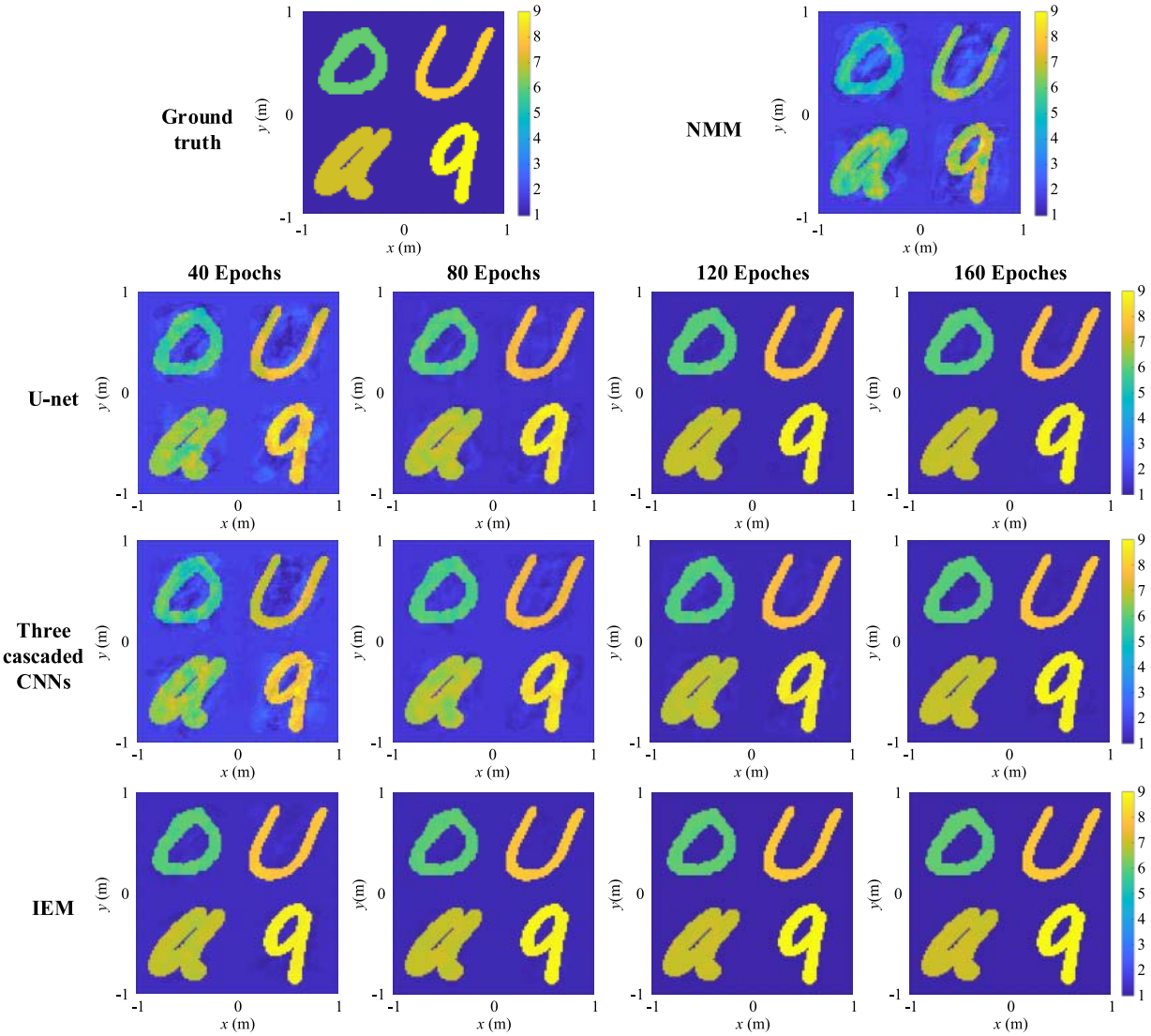

Fig. 11. Ground truth, reconstructed 2-D images by NMM, U-net, three cascaded CNNs, and the proposed IEM in different epochs based on the training results shown in Fig. 10.

Four different digits with different relative permittivities are randomly placed in the DOI. The relative permittivity values are in the range of [6 9]. Hundred samples produced by the NMM are employed to train the U-Net, three cascaded CNNs, and the IEM proposed in this article. The variations of model misfits in the training are shown in Fig. 10. We can see that the training of the IEM converges much faster than those of U-Net and cascaded CNNs although the final data misfits of these three methods are almost the same. More detailed comparisons of training time and model misfits in different epochs for three methods are listed in Table IV. The low training cost of the IEM is due to its much simpler architecture than those of the U-Net in [27] and the three cascaded CNNs in [26]. As mentioned in Section III-A, because the NMM can obtain the preliminary images of the scatterers with a higher accuracy compared with BP, the IEM used in this article is constructed simply, and thus, the training cost is reduced significantly.

We then test the U-Net, cascaded CNNs, and IEM using a preliminary image including four handwriting digits generated by the NMM. The ground truth and the preliminary images are shown in the first row of Fig. 11. The reconstructed images based on the training results in different epochs by three different methods are shown from the first column to the fourth column in the second row to the fourth row. The corresponding model misfits are listed in Table V. The reconstructed image by the IEM is good enough in the 40th epoch. By contrast, the cascaded CNNs and U-net could obtain the same level performance after 160 epochs. Clearly, the proposed IEM has a lower training cost.

VII. Conclusion and Future Work

In this article, a dual-module NMM-IEM machine learning scheme is developed to deal with the reconstruction of inhomogeneous scatterers with high contrasts and large electrical dimensions. Compared with the previous works regarding the applications of CNNs to EM inversion, the ELM and a CNN with low training costs are used in the proposed modules. Because the weight matrices of the ELM are only solved once using all the training samples, the ELM is trained within 1 s for all the numerical cases presented in this article. Although

TABLE IV

TRAINING RESULTS OF U-NET, THREE CASCADED CNNS, AND THE PROPOSED IEM WITH 100 SAMPLES GENERATED FROM NMM

Epoch	Training time (second)			Model misfit (%)		
	U-Net	Cascaded CNNs	IEM	U-Net	Cascaded CNNs	IEM
40	114	164	10	8.65	8.15	2.19
80	226	329	18	5.11	6.50	1.66
120	337	494	28	1.31	2.74	1.47
160	453	659	39	1.21	1.51	1.49

TABLE V

INVERSION MODEL MISFITS (%) OF U-NET, CASCADED CNNS, AND THE PROPOSED IEM IN DIFFERENT EPOCHS SHOWN IN FIG. 11

Epoch	U-net	Cascaded CNNs	IEM
40	8.86	8.61	2.11
80	5.21	6.18	1.56
120	1.64	2.89	1.47
160	1.52	1.46	1.48

having the low training cost, the ELM can reconstruct the preliminary images of the unknown scatterers with a much higher accuracy than the BP method employed in the previous works. Based on the good results from NMM containing the ELM, the following CNN with a simple architecture in the IEM also can be trained at a low cost and is able to improve further the inversion results from the NMM.

The numerically simulated data and the experimental data measured in the laboratory are employed to test the proposed scheme. It is found that the performance of the NMM-IEM is independent of the electrical sizes and contrasts, which is quite different from the conventional methods, e.g., VBIM. The antinoise ability tests show that the model misfit of the reconstruction can be as low as 16% even when the contrast is 7, and the measured data are contaminated by 10 dB noise. In addition, the antinoise ability is also independent of the electrical sizes and contrasts. The reconstruction of the scattered field data for two disks provided by Institute Fresnel demonstrates the adaptability of the dual-module scheme for high-frequency data measured in the laboratory. Finally, by comparing the IEM with the U-Net and three cascaded CNNs used in the previous works, we find that the training of the CNN in the IEM has a much lower cost than the training of U-Net and three cascaded CNNs. The key reason is that the NMM itself can provide the preliminary images with the relatively high accuracy, and thus, the architecture of the CNN in the IEM is rather simple.

The future work will be focused on two aspects.

1) Reconstruct multiple parameters by the proposed dual-module scheme. In our previous work, the simultaneous reconstruction of the 18 model parameters of the arbitrary anisotropic scatterers has been accomplished by using the conventional iterative method VBIM [39]. Therefore, in the future work, we will first apply the NMM-IEM to the scatterers with both permittivity and conductivity and then to the anisotropic scatterers.
2) Explore the inversion performance of the dual-module scheme. A heuristic work has been accomplished in [40] for the CNN. However, the ELM lacks the iterative training process. However, its stability of the output against the input perturbation can be further studied, which is important when the input data are contaminated by noise.

REFERENCES

[1] D. Colton and R. Kress, Eds., *Inverse Acoustic and Electromagnetic Scattering Theory*. New York, NY, USA: Springer, 1998.

[2] M. S. Zhdanov, Ed., *Geophysical Inverse Theory and Regularization Problems*. Amsterdam, The Netherlands: Elsevier, 2004.

[3] S. Caorsi, A. Massa, M. Pastorino, and M. Donelli, "Improved microwave imaging procedure for nondestructive evaluations of two-dimensional structures," *IEEE Trans. Antennas Propag.*, vol. 52, no. 6, pp. 1386–1397, Jun. 2004.

[4] L.-P. Song, C. Yu, and Q. H. Liu, "Through-wall imaging (TWI) by radar: 2-D tomographic results and analyses," *IEEE Trans. Geosci. Remote Sens.*, vol. 43, no. 12, pp. 2793–2798, Dec. 2005.

[5] A. Abubakar, P. M. van den Berg, and J. J. Mallorqui, "Imaging of biomedical data using a multiplicative regularized contrast source inversion method," *IEEE Trans. Microw. Theory Techn.*, vol. 50, no. 7, pp. 1761–1771, Jul. 2002.

[6] P. M. Meaney, M. W. Fanning, S. P. P. D. Li, and K. D. Paulsen, "A clinical prototype for active microwave imaging of the breast," *IEEE Trans. Microw. Theory Techn.*, vol. 48, no. 11, pp. 1841–1853, Nov. 2000.

[7] T. Jun Cui, W. C. Chew, A. A. Aydiner, and S. Chen, "Inverse scattering of two-dimensional dielectric objects buried in a lossy Earth using the distorted born iterative method," *IEEE Trans. Geosci. Remote Sens.*, vol. 39, no. 2, pp. 339–346, Feb. 2001.

[8] A. Kirsch, Ed., *An Introduction to the Mathematical Theory of Inverse Problems*. New York, NY, USA: Springer-Verlag, 1996.

[9] Y. M. Wang and W. C. Chew, "An iterative solution of the two-dimensional electromagnetic inverse scattering problem," *Int. J. Imag. Syst. Technol.*, vol. 1, no. 1, pp. 100–108, 1989.

[10] T. M. Habashy, M. L. Oristaglio, and A. T. de Hoop, "Simultaneous nonlinear reconstruction of two-dimensional permittivity and conductivity," *Radio Sci.*, vol. 29, no. 4, pp. 1101–1118, Jul. 1994.

[11] P. M. V. D. Berg and R. E. Kleinman, "A contrast source inversion method," *Inverse Problems*, vol. 13, no. 6, pp. 1607–1620, Dec. 1997.

[12] P. M. V. D. Berg, A. L. V. Broekhoven, and A. Abubakar, "Extended contrast source inversion," *Inverse Problems*, vol. 15, no. 5, pp. 1325–1344, Oct. 1999.

[13] X. Chen, "Subspace-based optimization method for solving inverse-scattering problems," *IEEE Trans. Geosci. Remote Sens.*, vol. 48, no. 1, pp. 42–49, Jan. 2010.

[14] Y. Zhong and X. Chen, "An FFT twofold subspace-based optimization method for solving electromagnetic inverse scattering problems," *IEEE Trans. Antennas Propag.*, vol. 59, no. 3, pp. 914–927, Mar. 2011.

[15] K. Xu, Y. Zhong, and G. Wang, "A hybrid regularization technique for solving highly nonlinear inverse scattering problems," *IEEE Trans. Microw. Theory Techn.*, vol. 66, no. 1, pp. 11–21, Jan. 2018.

[16] K. Belkebir, P. C. Chaumet, and A. Sentenac, "Superresolution in total internal reflection tomography," *J. Opt. Soc. Amer. A, Opt. Image Sci.*, vol. 22, no. 9, pp. 1889–1897, Sep. 2005.

[17] T. M. Habashy, R. W. Groom, and B. R. Spies, "Beyond the born and Rytov approximations: A nonlinear approach to electromagnetic scattering," *J. Geophys. Res., Solid Earth*, vol. 98, no. B2, pp. 1759–1775, Feb. 1993.

[18] Z. Q. Zhang and Q. H. Liu, "Reconstruction of axisymmetric media with an FFHT-enhanced extended born approximation," *Inverse Problems*, vol. 16, no. 5, pp. 1281–1295, Oct. 2000.

[19] A. Krizhevsky, I. Sutskever, and G. E. Hinton, "ImageNet classification with deep convolutional neural networks," in *Proc. 25th Int. Conf. Neural Inf. Process. Syst.*, 2012, pp. 1097–1105.

[20] O. Russakovsky *et al.*, "ImageNet large scale visual recognition challenge," *Int. J. Comput. Vis.*, vol. 115, no. 3, pp. 211–252, Dec. 2015.

[21] R. Girshick, J. Donahue, T. Darrell, and J. Malik, "Rich feature hierarchies for accurate object detection and semantic segmentation," in *Proc. IEEE Conf. Comput. Vis. Pattern Recognit.*, Jun. 2014, pp. 580–587.

[22] O. Ronneberger, P. Fischer, and T. Brox, "U-net: Convolutional networks for biomedical image segmentation," in *Proc. 18th Int. Conf. Med. Image Comput. Comput.-Assist. Intervent.*, 2015, pp. 234–241.

[23] D. Eigen, C. Puhrsch, and R. Fergus, "Depth map prediction from a single image using a multi-scale deep network," in *Proc. Adv. Neural Inf. Process. Syst.*, 2014, pp. 2366–2374.

[24] S. Caorsi and P. Gamba, "Electromagnetic detection of dielectric cylinders by a neural network approach," *IEEE Trans. Geosci. Remote Sens.*, vol. 37, no. 2, pp. 820–827, Mar. 1999.
[25] I. T. Rekanos, "Neural-network-based inverse-scattering technique for online microwave medical imaging," *IEEE Trans. Magn.*, vol. 38, no. 2, pp. 1061–1064, Mar. 2002.
[26] L. Li, L. G. Wang, F. L. Teixeira, C. Liu, A. Nehorai, and T. J. Cui, "DeepNIS: Deep neural network for nonlinear electromagnetic inverse scattering," *IEEE Trans. Antennas Propag.*, vol. 67, no. 3, pp. 1819–1825, Mar. 2019.
[27] Z. Wei and X. Chen, "Deep-learning schemes for full-wave nonlinear inverse scattering problems," *IEEE Trans. Geosci. Remote Sens.*, vol. 57, no. 4, pp. 1849–1860, Apr. 2019.
[28] Z. Wei and X. Chen, "Physics-inspired convolutional neural network for solving full-wave inverse scattering problems," *IEEE Trans. Antennas Propag.*, vol. 67, no. 9, pp. 6138–6148, Sep. 2019.
[29] H. M. Yao, W. E. I. Sha, and L. Jiang, "Two-step enhanced deep learning approach for electromagnetic inverse scattering problems," *IEEE Antennas Wireless Propag. Lett.*, vol. 18, no. 11, pp. 2254–2258, Nov. 2019.
[30] R. Guo, X. Song, M. Li, F. Yang, S. Xu, and A. Abubakar, "Supervised descent learning technique for 2-D microwave imaging," *IEEE Trans. Antennas Propag.*, vol. 67, no. 5, pp. 3550–3554, May 2019.
[31] G.-B. Huang, Q.-Y. Zhu, and C.-K. Siew, "Extreme learning machine: Theory and applications," *Neurocomputing*, vol. 70, nos. 1–3, pp. 489–501, Dec. 2006.
[32] T. Lan, N. Liu, Y. Liu, F. Han, and Q. H. Liu, "2-D electromagnetic scattering and inverse scattering from magnetodielectric objects based on integral equation method," *IEEE Trans. Antennas Propag.*, vol. 67, no. 2, pp. 1346–1351, Feb. 2019.
[33] W. C. Chew, *Waves Fields Inhomogeneous Media*. New York, NY, USA: IEEE Press, 1995, ch. 9.
[34] M.-B. Li, G.-B. Huang, P. Saratchandran, and N. Sundararajan, "Fully complex extreme learning machine," *Neurocomputing*, vol. 68, pp. 306–314, Oct. 2005.
[35] J. Xiao, J. Li, Y. Chen, F. Han, and Q. H. Liu, "Fast electromagnetic inversion of inhomogeneous scatterers embedded in layered media by born approximation and 3-D U-net," *IEEE Geosci. Remote Sens. Lett.*, early access, Nov. 28, 2019, doi: 10.1109/LGRS.2019.2953708..
[36] R. Hecht-Nielsen, "Kolmogorov's mapping neural network existence theorem," in *Proc. IEEE Conf. Neural Netw.*, New York, NY, USA, 1987, pp. 11–13.
[37] J.-M. Geffrin, P. Sabouroux, and C. Eyraud, "Free space experimental scattering database continuation: Experimental set-up and measurement precision," *Inverse Problems*, vol. 21, no. 6, pp. S117–S130, Dec. 2005.
[38] Y. Lecun, L. Bottou, Y. Bengio, and P. Haffner, "Gradient-based learning applied to document recognition," *Proc. IEEE*, vol. 86, no. 11, pp. 2278–2324, Nov. 1998.
[39] J. Li, J. Zhuo, Z. Guan, F. Han, and Q. H. Liu, "3-D electromagnetic scattering and inverse scattering by magnetodielectric objects with arbitrary anisotropy in layered uniaxial media," *IEEE Trans. Antennas Propag.*, vol. 68, no. 2, pp. 1009–1022, Feb. 2020.
[40] L. Li, L. G. Wang, and F. L. Teixeira, "Performance analysis and dynamic evolution of deep convolutional neural network for electromagnetic inverse scattering," *IEEE Antennas Wireless Propag. Lett.*, vol. 18, no. 11, pp. 2259–2263, Nov. 2019.

Li-Ye Xiao (Member, IEEE) received the B.S. and Ph.D. degrees in electronic information science and technology from the University of Electronic Science and Technology of China (UESTC), Chengdu, China, in 2015 and 2019, respectively.

In 2018, he was a Visiting Scholar with the Department of Electrical and Computer Engineering, Duke University, Durham, NC, USA. Currently, he is with the Institute of Electromagnetics and Acoustics, Xiamen University, Xiamen, China, as a Post-Doctoral Researcher. His current research interest is computational electromagnetics.

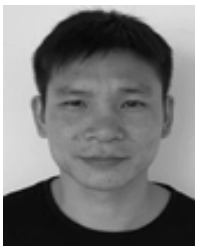

Jiawen Li received the B.S. and M.S. degrees in electronic science and technology from the Wuhan University of Technology of China, Wuhan, China, in 2011 and 2016, respectively. He is currently pursuing the Ph.D. degree with Xiamen University, Xiamen, China.

His research interests include electromagnetic scattering and inverse scattering in complex media and the full-wave inversion of anisotropic targets.

Feng Han (Member, IEEE) received the B.S. degree in electronic science from Beijing Normal University, Beijing, China, in 2003, the M.S. degree in geophysics from Peking University, Beijing, in 2006, and the Ph.D. degree in electrical engineering from Duke University, Durham, NC, USA, in 2011.

He is currently an Assistant Professor with the Institute of Electromagnetics and Acoustics, Xiamen University, Xiamen, China. His research interests include ionosphere remote sensing by radio atmospherics, electromagnetic full-wave inversion by integral equations, reverse time migration image, and the design of an electromagnetic detection system.

Wei Shao (Member, IEEE) received the B.E. degree in electrical engineering and the M.Sc. and Ph.D. degrees in radio physics from UESTC, Chengdu, China, in 1998, 2004, and 2006, respectively.

He joined UESTC in 2007, where he is currently a Professor. From 2010 to 2011, he was a Visiting Scholar with the Electromagnetic Communication Laboratory, Pennsylvania State University, State College, PA, USA. From 2012 to 2013, he was a Visiting Scholar with the Department of Electrical and Electronic Engineering, The Hong Kong University, Hong Kong. His current research interests include computational electromagnetics and antenna design.

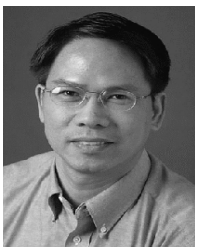

Qing Huo Liu (Fellow, IEEE) received the B.S. and M.S. degrees in physics from Xiamen University, Xiamen, China, and the Ph.D. degree in electrical engineering from the University of Illinois at Urbana–Champaign, Champaign, IL, USA.

From September 1986 to December 1988, he was a Research Assistant with the Electromagnetics Laboratory, University of Illinois at Urbana–Champaign, where he was a Post-Doctoral Research Associate from January 1989 to February 1990. He was a Research Scientist and the Program Leader with Schlumberger-Doll Research, Ridgefield, CT, USA, from 1990 to 1995. From 1996 to May 1999, he was an Associate Professor with New Mexico State University, Las Cruces, NM, USA. Since June 1999, he has been with Duke University, Durham, NC, USA, where he is currently a Professor of electrical and computer engineering. He has also been the Founder and Chairman of Wave Computation Technologies, Inc., since 2005. His research interests include computational electromagnetics and acoustics, inverse problems, and their application in nanophotonics, geophysics, biomedical imaging, and electronic packaging. He has published widely in these areas.

Dr. Liu is a fellow of the Acoustical Society of America, the Electromagnetics Academy, and the Optical Society of America. He received the 1996 Presidential Early Career Award for Scientists and Engineers (PECASE) from the White House, the 1996 Early Career Research Award from the Environmental Protection Agency, the 1997 CAREER Award from the National Science Foundation, the 2017 Technical Achievement Award, the 2018 Computational Electromagnetics Award from the Applied Computational Electromagnetics Society, the 2018 Harrington-Mittra Award in Computational Electromagnetics from the IEEE Antennas and Propagation Society, and the ECE Distinguished Alumni Award from the University of Illinois at Urbana–Champaign in 2018. He has served as an IEEE Antennas and Propagation Society Distinguished Lecturer and the Founding Editor-in-Chief for the *IEEE Journal on Multiscale and Multiphysics Computational Techniques*.